# Energy partition at collisionless supercritical quasiperpendicular shocks

**Steven J Schwartz[1*†], Katherine A Goodrich[2], Lynn B Wilson III[3], Drew L Turner[4], Karlheinz J Trattner[1], Harald Kucharek[5], Imogen Gingell[6], Stephen A Fuselier[7,8], Ian J Cohen[4], Hadi Madanian[1], Robert E Ergun[1], Daniel J Gershman[3], Robert J Strangeway[9]**

[1]Laboratory for Atmospheric and Space Physics, CU Boulder, Boulder, CO
[2]Deptartment of Physics and Astronomy, West Virginia University, Morgantown, WV
[3]Goddard Space Flight Center, Greenbelt, MD
[4]Space Exploration Sector, The Johns Hopkins Applied Physics Laboratory, Laurel, MD
[5]University of New Hampshire, Durham, NH
[6]School of Physics and Astronomy, University of Southampton, Southampton, UK
[7]Southwest Research Institute, San Antonio, TX
[8]The University of Texas at San Antonio, San Antonio, TX USA
[9]UCLA, Los Angeles, CA

**Key Points:**

- We establish and apply a framework to quantify total energy partition across collisionless shocks.
- The fragmented suprathermal ions at the shock and downstream dominate the energy budget.
- Present instrument limitations suggest a roadmap for next generation shock-dedicated space missions.

Manuscript Date 7 May 2022

*Laboratory for Atmospheric and Space Physics, CU Boulder, Boulder, CO
†Also Emeritus Professor, Imperial College London

Corresponding author: Steven Schwartz, steven.schwartz@lasp.colorado.edu

## Abstract

Collisionless shocks in astrophysical plasmas are important thermalizers, converting some of the incident flow energy into thermal energy, and non-thermalizers, partitioning that energy in unequal ways to different particle species, sub-populations thereof, and field components. This partition problem, or equivalently the shock equation of state, lies at the heart of shock physics. Here we employ systematically a framework to capture all the incident and downstream energy fluxes at two example traversals of the Earth's bow shock by the Magnetospheric Multiscale Mission. Here and traditionally such data has to be augmented by information from other spacecraft, e.g., to provide more accurate measurements of the cold solar wind beam. With some care and fortuitous choices, the energy fluxes are constant, including instantaneous measurements through the shock layer. The dominant incident proton ram energy is converted primarily into downstream proton enthalpy flux, the majority of which is actually carried by a small fraction of suprathermal protons. Fluctuations include both real and instrumental effects. Separating these, resolving the solar wind beam, and other considerations point the way to a dedicated mission to solve this energy partition problem across a full range of plasma and shock conditions.



## Plain Language Summary

Explosions and fast flows in astrophysical environments lead to the formation of shock waves, the role of which is to process the energy incident upon them. In most astrophysical plasmas, the densities are so low that particle collisions are negligibly rare. Such plasmas are incapable of establishing an equilibrium at a constant temperature across electron and ion species. Astrophysical shocks therefore channel some of that incident energy, for example, to accelerate high energy cosmic rays, and otherwise partition the energy amongst the plasma's many constituents. This paper addresses from a holistic approach this partition problem by employing a mathematical framework to analyze data from state of the art spacecraft that traverse shock waves in interplanetary space. We successfully verify, with some assumptions, overall energy conservation. We also identify sub-portions and features of the proton population that receive a disproportionate share of the incident energy. The approach naturally highlights the critical measurements and reveals limitations of using some instruments in regimes for which they were not de-

signed. A dedicated satellite mission to study shock physics would overcome these difficulties.

## 1 Introduction

Shock waves in astrophysical plasmas are almost always operating on scales that are much smaller than the particle collisional mean free path. Such collisionless shocks require plasma kinetic processes to decelerate the incident bulk flow and "dissipate" that incident energy flux. These processes operate differently on the different plasma species and electromagnetic fields, and over different scales. They are responsible for preferential heating together with the acceleration to high energies of sub-populations of particles (Kucharek et al., 2003). This unknown partitioning of the incident energy lies at the heart of the shock problem. The bow shock formed by the interaction of the supersonic solar wind flow with the Earth's magnetosphere has long been a prime laboratory for investigating collisionless shock physics thanks to its accessibility by ever-increasingly high quality in situ satellite observations (Burgess & Scholer, 2015; Schwartz, 2006; Schwartz et al., 2013; Krasnoselskikh et al., 2013; Tsurutani & Stone, 1985; Stone & Tsurutani, 1985; Scudder, Mangeney, Lacombe, Harvey, Wu, & Anderson, 1986).

Most shock studies have concentrated on a variety of processes that are believed to play a role in the collisionless shock problem, including ion reflection (Woods, 1969; Paschmann et al., 1982; Sckopke et al., 1983), DC fields (Scudder, Mangeney, Lacombe, Harvey, & Aggson, 1986; Gedalin, 2020; Schwartz et al., 2021), micro-instabilities and turbulence (Scudder, Mangeney, Lacombe, Harvey, & Aggson, 1986; Wilson et al., 2014; Goodrich et al., 2018), particle acceleration (Amano et al., 2020; Kucharek et al., 2004; Kis et al., 2004), non-stationarity/shock reformation (Johlander et al., 2018; Madanian, Desai, et al., 2021), magnetic reconnection (Gingell et al., 2019, 2020; Wang et al., 2019) and others. Some statistical studies have focused on isolated aspects of the partition problem, such as the parametric dependence of the downstream electron temperature on upstream conditions (Schwartz et al., 1988), the statistics of electron distribution functions at interplanetary shocks (Wilson et al., 2019b, 2019a, 2020), the percentage of reflected ions as a function of Mach number (Leroy et al., 1982), or the amount of energy given to energetic particles (David et al., 2022). In such studies, the basic shock parameters (Mach number, plasma $\beta$, shock geometry, electron to ion temperature ratio) are eval-

uated through careful use of the Rankine Hugoniot fluid shock jump conditions to supplement and cross-check observed quantities.

While we have learned much about the physics of collisionless shocks through such studies, the fundamental energy partition problem has been somewhat neglected. This is due, perhaps, to the comprehensive and accurate simultaneous measurements that are required to fully characterize the upstream and downstream states. For example, the dominant energy flux incident on the bow shock is the solar wind proton ram energy, and the dominant downstream energy flux is the result of proton heating by the shock reflection and other processes. However the total energy budget includes nonthermal features in both the upstream and downstream proton distributions together with other particle species (electrons, $\alpha$-particles and other minor ions), accelerated sub-populations of particles, and DC and AC Poynting fluxes. For some contexts, such as astrophysical cosmic ray production, it is important not just to know the dominant energy flux carriers but also, e.g., the energetic particle fluxes and their dependencies on shock parameters.

These considerations lead us to lay down a comprehensive framework for keeping track of as many different energy fluxes as possible and to study their variability with shock parameters. This approach is challenging at even the most accessible of shocks, the terrestrial bow shock, for several reasons. Resolving the cold, super-thermal solar wind proton beam and tracking the proton velocity distributions as they get ripped apart, mixed and partially thermalized through and downstream of the shock requires dedicated and well-cross-calibrated solar wind and $4\pi$ detectors not available on most modern space plasma missions. Measuring the Poynting flux requires good 3D electric and magnetic field measurements, both AC and DC. Resolving velocity space features of $\alpha$-particles and other minor species in the solar wind is challenging. Critically, evaluating the kinetic processes responsible for the energy partition through the shock transition layer demands electron scale (1 s or less) temporal resolution for most parameters. No current space mission can make all these measurements simultaneously; ideally to remove any contextual temporal variability it should be done simultaneously both upstream and downstream of the shock.

Current studies (Goodrich et al., 2022, private communication) are looking into designing a dedicated mission to attack the shock partition comprehensively. In order to

inform those considerations, we attempt here to exploit the high-quality, high-resolution data from the Magnetospheric Multiscale Mission (MMS) (Burch et al., 2016) in order to demonstrate what can, and cannot, currently be accomplished. MMS was designed to study hot magnetospheric plasmas. The low density and cold nature of the solar wind leads to some uncertainties and errors in determining the full set of parameters needed for the partition problem. Some contributions of the different species, such as the heating at low particle energies or the nature of accelerated beams or distribution tails, also stretch signal-to-noise aspects due to a combination of background and counting statistics. Despite these limitations, we shall see that MMS can shed considerable light onto the shock partition problem thanks to its comprehensive instrument suite and high time resolution.

The next sections summarize the data and our primary analysis methods. We then present our results and provide some discussion before drawing our final Conclusions.

## 2 Data

Our primary results are drawn from the Magnetospheric Multiscale mission (MMS) (Burch et al., 2016). We also used data from the Wind (Harten & Clark, 1995; L. B. Wilson et al., 2021) spacecraft to establish the prevailing interplanetary conditions. The main analysis relies on MMS data from the Fast Plasma Investigation (FPI) (Pollock et al., 2016), Fluxgate Magnetometer (FGM) (Russell et al., 2016), electric field instrumentation (Torbert et al., 2016; Ergun et al., 2016; Lindqvist et al., 2016) and Hot Particle Composition Analyzer (HPCA)(Young et al., 2017). Where possible, we used moment sums provided by the FPI team in the public L2 data files. When we subset the particle populations we calculate proton moments above 25 eV in the spacecraft frame to minimize the impact of counting statistics at low energies.

We investigate in detail two crossings of the terrestrial bow shock by MMS to study the different energy fluxes incident on the shock and the resulting downstream partition of those fluxes. We also track those fluxes through the shock traversal as a first step in linking that partition to specific physical processes.

With even the state of the art instrumentation provided by MMS, we are forced to make some assumptions in order to compile a full set of energy fluxes. These are elaborated in the setup and discussion of each example.

## 3 Mathematical framework

In order to assess the full partition it is necessary to establish the mathematical framework for a multi-component plasma. To do this, we review the moment analysis of the collisionless Vlasov equation for the velocity distribution function $f(\mathbf{v})$ of each species $j$ (Boyd & Sanderson, 2003; Schwartz, 1998; Paschmann & Daly, 2008; Schwartz & Marsch, 1983). For convenience, we omit the species label $j$ unless we need to refer to a specific species. We use "species" here in a generalized way, since it is often convenient to separate the protons, for example, into different sub-populations, such as the core solar wind, shock-reflected ions, and diffuse energetic ions. We treat each of these populations as a separate species. Note that since protons can be exchanged amongst these different sub-populations, the continuity equation expressing conservation of protons applies only to their aggregate, not to each sub-population.

The velocity-space average of any quantity $A(\mathbf{v}, \mathbf{x}, t)$ is given by

$$\langle A \rangle \equiv \frac{1}{n} \int A f(\mathbf{v})\, d^3v \tag{1}$$

where $n$ is the number density of the species whose phase space density is $f(\mathbf{v})$.

We define $\mathbf{U}$ as a convenient reference velocity common to all species. In some contexts this might be the total center of mass velocity, or the velocity of one of the plasma constituents. We then decompose a particle velocity $\mathbf{v}$ as

$$\mathbf{v} = \mathbf{U} + \mathbf{u}_j + \mathbf{w} \tag{2}$$

with the peculiar velocity $\mathbf{w}$ defined such that $\langle \mathbf{w} \rangle \equiv \mathbf{0}$. For each species, the velocity $\mathbf{u}$ (subscript $j$ omitted for brevity) is the species' bulk velocity relative to the reference velocity $\mathbf{U}$. We note here that while $\mathbf{U}$ is common to all species, many have relative drifts with respect to one another, so their $\mathbf{u}_j$'s will be different. Such differential drifts can be an important part of the energy associated with that species (Schwartz & Marsch, 1983; Goldman et al., 2020, 2021). Unless the differential streaming between species needs to be studied explicitly, the overall energetics only involve the species' total bulk velocity $\mathbf{u}' \equiv \mathbf{U} + \mathbf{u}$.

The framework below can be applied in any frame in which the shock is at rest, to meet the temporal stationarity requirement. For the shock application, we choose to evaluate energy fluxes in the Normal Incidence Frame (NIF), in which the upstream (solar wind proton) flow is along the shock normal. Velocities measured in the spacecraft

frame are transformed to the NIF frame by subtracting the velocity

$$\mathbf{V}^{SC2NIF} = V_n^{sh}\mathbf{n} + \mathbf{V}^{up,SC} - \mathbf{n}\left(\mathbf{V}^{up,SC}\cdot\mathbf{n}\right) \tag{3}$$

where $V_n^{sh}$ is the signed shock velocity along the shock normal $\mathbf{n}$, and $\mathbf{V}^{up,SC}$ is the incident bulk flow velocity in the spacecraft frame, which we take to be the solar wind proton velocity (see Figure 1c and Equation 5 in Schwartz et al. (2021)). Then $\mathbf{u}'$ will be the species' bulk velocity measured in the NIF frame.

With this decomposition, we define in Table 1 the fluid-like quantities for each species.

**Table 1.** Moment definitions

| Symbol | Definition | Name |
|---|---|---|
| $n$ | $\int f(\mathbf{v})\, d^3v$ | number density |
| $\rho$ | $nm$ | mass density |
| $\mathbf{u}$ | $\langle\mathbf{v}\rangle - \mathbf{U}$ | Relative bulk velocity |
| $\underline{\underline{\mathbf{p}}}$ | $\rho\langle\mathbf{ww}\rangle$ | Pressure tensor |
| $p$ | $\frac{1}{3}\rho\langle w^2\rangle \equiv \frac{1}{3}\mathrm{tr}\,\underline{\underline{\mathbf{p}}}$ | Scalar pressure |
| $\mathbf{q}$ | $\frac{1}{2}\rho\langle\mathbf{w}w^2\rangle$ | Heat flux |
| $\mathbf{Q}$ | $\rho\langle\mathbf{v}\frac{1}{2}v^2\rangle$ | Total energy flux |

It is straightforward to now write the total species energy flux $\mathbf{Q}$ in terms of the moments of $f(\mathbf{v})$ as

$$\begin{aligned}\mathbf{Q} &= \mathbf{q} + && (4)\\ &\quad + \underline{\underline{\mathbf{p}}}\cdot\mathbf{u}' + \frac{3}{2}p\mathbf{u}' + && (5)\\ &\quad + \mathbf{u}'\frac{1}{2}\rho u'^2 && (6)\end{aligned}$$

The combination of the two terms in (5) defines the enthalpy flux $\mathbf{F}_{\mathrm{enth}}$ while (6) is the bulk flow or ram energy flux $\mathbf{F}_{\mathrm{ram}}$. Note that for a species that contains two distinct sub-populations, for example, contributions of different terms in (4), (5) and (6) will be different if the sub-populations are considered separately or only the moments of the parent species are considered. However, the total energy flux is the same.

The enthalpy flux can be expanded to reveal the contributions of, e.g., parallel and perpendicular pressures by decomposing the pressure tensor $\underline{\underline{\mathbf{p}}}$ as

$$\underline{\underline{\mathbf{p}}} \equiv p_{\parallel}\hat{\mathbf{b}}\hat{\mathbf{b}} + p_{\perp}\left(\underline{\underline{\mathbf{I}}} - \hat{\mathbf{b}}\hat{\mathbf{b}}\right) + \underline{\underline{\mathbf{p}}}^{\dagger} \tag{7}$$

which identifies the scalar parallel (perpendicular) pressure $p_{\parallel}$ ($p_{\perp}$) with

$$p_{\parallel} \equiv \hat{\mathbf{b}}^T \cdot \underline{\underline{\mathbf{p}}} \cdot \hat{\mathbf{b}} \tag{8}$$

$$p_{\perp} \equiv \frac{1}{2}\left(tr\,\underline{\underline{\mathbf{p}}} - p_{\parallel}\right) \tag{9}$$

where $\hat{\mathbf{b}}$ is a unit (column) vector in the direction of the local magnetic field. The traceless tensor $\underline{\underline{\mathbf{p}}}^{\dagger}$ ensures completeness and is found by re-arranging (7) once $p_{\parallel}$ and $p_{\perp}$ are determined from (8) and (9). It embodies the influence of agyrotropy and any other effects on the structure of the full pressure tensor. Substituting this expression for $\underline{\underline{\mathbf{p}}}$ into (5) yields

$$\mathbf{F}_{enth} = p_{\parallel}\left[\frac{1}{2}\mathbf{u}' + \hat{\mathbf{b}}\left(\hat{\mathbf{b}}\cdot\mathbf{u}'\right)\right] + \tag{10}$$

$$+p_{\perp}\left[2\mathbf{u}' - \hat{\mathbf{b}}\left(\hat{\mathbf{b}}\cdot\mathbf{u}'\right)\right] + \tag{11}$$

$$+\underline{\underline{\mathbf{p}}}^{\dagger}\cdot\mathbf{u}' \tag{12}$$

Interestingly, under nearly perpendicular geometries $\hat{\mathbf{b}}\cdot\mathbf{u}'$ is small and the perpendicular pressure is weighted by a factor of 4 relative to the parallel contribution to the total enthalpy flux.

To the particle kinetic energy fluxes we add the electromagnetic Poynting flux $\mathbf{E}\times\mathbf{B}/\mu_o$. Steady-state energy conservation requires that the total energy flux $\mathbf{F}$ along the shock normal be constant, i.e.,

$$\mathbf{F}\cdot\mathbf{n} \equiv \mathbf{n}\cdot\frac{\mathbf{E}\times\mathbf{B}}{\mu_o} + \sum_{\text{species}}\mathbf{Q}\cdot\mathbf{n} = \text{constant} \tag{13}$$

For shocks which exhibit non-stationary or spatial structure it may be useful to further expand all quantities in terms of spatio-temporal average and fluctuating contributions. This expansion applies also to the shock normal $\mathbf{n}$ in the case of rippled or reforming shocks (Lowe & Burgess, 2003; Johlander et al., 2018; Madanian, Desai, et al., 2021). Under such circumstances, $\mathbf{F}\cdot\mathbf{n}$ need no longer be constant, due to the localized or temporal build up/depletion of energy density. Nonetheless, it is instructive to explore the various contributions to the energy flux, suitably averaged to minimize the impact of variations in $\mathbf{n}$ or other spatial/temporal variations (see Zank et al. (2021) for a partial relaxation of these restrictions).

# 4 Example 1: 2019-03-05 at 19:39

## 4.1 Average parameters

This shock crossing was analyzed in the detailed study of the electrostatic cross-shock potential by Schwartz et al. (2021). Here we need a wider set of parameters measured on both sides of the shock. We have revisited all the datasets, and provide in Table 2 a summary of all the parameters needed to evaluate (13). The extensive footnotes to that table document the uncertainties, assumptions, and in some cases guesses forced on us due to the unavailability of definitive accurate parameter values.

Table 2: Parameters for MMS[a] shock crossing on 2019-03-05 @ 19:39

| Parameter | Upstream (up) | Downstream (dn) | Comments |
|---|---|---|---|
| MMS Times | 19:43:57-19:44:47 | 19:34:49-19:36:53 | up: MMS2; dn: MMS1 |
| Wind Times | 18:15:35-18:16:15 | | |
| MMS Position | (10.1, -13.4, 6.9)[b] | | $R_e$ |
| Shock normal | (0.847, -0.482, 0.226) | | Slavin and Holzer (1981) |
| $V_n^{sh}$ | -7.6 | | MMS2,1,4 timing |
| $\mathbf{V}^{SC2NIF}$ | (-113, -150, 72) | | km/s Eqn (3) |
| Shock geometry $\theta_{Bn}$ | 76° | | |
| Shock $M_A$ | 7.4 | | |
| Shock $M_{fast}$ | 5.6 | | |
| Upstream plasma $\beta_{i,e}$ | 0.54, 0.41 | | |
| Magnetic field $\mathbf{B}$ | (3.45, 2.47, -2.46)[b] | (9.48, 9.9, -8.1) | nT; $\mathbf{B}_{up}$ MMS2 |
| DC Electric Field[c] | (0.21, 0.98, 1.28) | (-0.46, 0.75, 1.46) | mV/m ($-\mathbf{u}'_p \times \mathbf{B}$) |
| Proton density $n_p$ | 5.3[d] | 17.1 | #/cm$^3$ |
| Proton velocity $\mathbf{V}_p$ | (-402, 14, -5)[e] | (-198, -85, 65) | km/s s/c frame |
| p NIF velocity $\mathbf{u}'_p$ | (-289, 164, -77) | (-85, 65, -7) | km/s |
| Proton pressure $\underline{\underline{\mathbf{p}}}_p$ | 0.0052[f] | $\begin{pmatrix} 0.47 & -0.08 & 0.05 \\ -0.08 & 0.36 & 0.04 \\ 0.05 & 0.04 & 0.48 \end{pmatrix}$ | nPa |
| Proton heat flux $q_p$ | (0 , 0, 0)[g] | (1.1, 7.2, -3.25) | $\mu$W/m$^2$ |
| Alpha density $n_\alpha$ | 0.024[h] | 0.12 | #/cm$^3$ |
| Alpha velocity $\mathbf{V}_\alpha$ | (-426, 8.7, 8.4)[i] | (-145, -63, 59) | km/s s/c frame |

Table 2: Parameters for MMS[a] shock crossing on 2019-03-05 @ 19:39 (cont.)

| Parameter | Upstream (up) | Downstream (dn) | Comments |
|---|---|---|---|
| $\alpha$ NIF velocity $\mathbf{u}'_\alpha$ | (-313, 159, -64) | (-32, 87, -13) | km/s |
| Alpha pressure $\underline{\underline{\mathbf{p}}}_\alpha$ | 0.06[j] | $\begin{pmatrix} 18 & 1 & 2 \\ 1 & 12 & 2 \\ 2 & 2 & 11 \end{pmatrix}$ | $10^{-3}$nPa |
| Alpha heat flux $q_\alpha$ | (0, 0, 0)[f] | (0, 0, 0)[f] | |
| Electron density $n_e$ | 5.35[k] | 16.7 | #/cm$^3$ |
| Electron velocity $\mathbf{V}_e$ | (-402.2, 14, -5)[l] | (-197, -84, 65) | km/s s/c frame |
| e$^-$ NIF velocity $\mathbf{u}'_e$ | (-289, 164, -77) | (-84, 66, -7) | km/s |
| Electron pressure $\underline{\underline{\mathbf{p}}}_e$ | 0.0038[e] | $\begin{pmatrix} 0.126 & -0.0001 & 0.0002 \\ -0.0001 & 0.126 & 10^{-5} \\ 0.0002 & 10^{-5} & 0.126 \end{pmatrix}$ | nPa |
| Electron heat flux $q_e$ | (0, 0, 0) | (0.2, 0.85, 0.68) | $\mu$W/m$^2$ |
| Energy fluxes along shock normal in $\mu$W/m$^2$ | | | |
| $\mathbf{F}_{\mathrm{ram,p}} \cdot \mathbf{n}$ | -175.4 | -17.2 | |
| $\mathbf{F}_{\mathrm{enth,p}} \cdot \mathbf{n}$ | -4.3 | -121.9 | |
| $\mathbf{q}_{\mathrm{p}} \cdot \mathbf{n}$ | 0 | -3.2 | |
| $\mathbf{F}_{\mathrm{ram},\alpha} \cdot \mathbf{n}$ | -3.7 | -0.3 | |
| $\mathbf{F}_{\mathrm{enth},\alpha} \cdot \mathbf{n}$ | -0.05 | -2.4 | |
| $\mathbf{q}_\alpha \cdot \mathbf{n}$ | 0 | 0 | |
| $\mathbf{F}_{\mathrm{ram,e}} \cdot \mathbf{n}$ | -0.1 | -0.01 | |
| $\mathbf{F}_{\mathrm{enth,e}} \cdot \mathbf{n}$ | -3.2 | -33.0 | |
| $\mathbf{q}_{\mathrm{e}} \cdot \mathbf{n}$ | 0 | -0.09 | |
| Poynting $\mathbf{E} \times \mathbf{B}/\mu_o$ | -6.2 | -21.0 | |
| Totals | -192.8 | -199.1 | |

[a] All downstream parameters from MMS1. Sources for most upstream parameters as footnoted or in Comments column.

[b] All vector and tensor components in GSE

[c] Assume DC $\mathbf{E} = -\mathbf{u}'_p \times \mathbf{B}$. Ignores Poynting flux carried by fluctuations

Table 2: Parameters for MMS[a] shock crossing on 2019-03-05 @ 19:39 (cont.)

| Parameter | Upstream (up) | Downstream (dn) | Comments |
|---|---|---|---|

[d] Derived from $n_p$(dn) using measured $\mathbf{u}'_p$(up,dn) assuming conservation of normal proton number flux. This value is consistent with Wind WAVES density deduced from upper hybrid resonance line.

[e] Wind 3DP.

[f] Wind SWE; isotropic contributions only.

[g] Unavailable

[h] Derived from $n_\alpha$(dn) using measured $\mathbf{u}'_\alpha$(up,dn) assuming conservation of normal $\alpha$ number flux.

[i] Wind onboard moment.

[j] No data available. Assume mean $T_\alpha/T_p \sim 2.5$ (L. B. Wilson III et al., 2018)

[k] Wind WAVES experiment upper hybrid line corresponds to $\sim 5\,\mathrm{cm}^{-3}$. Upstream value here ensures charge neutrality. Downstream value is actual MMS1 measured, and is close to neutrality.

[l] Derived from protons and alphas to ensure zero electric current.

The partition amongst the average upstream and downstream energy fluxes given in Table 2 are shown in Figure 1. Despite the assumptions, estimations and uncertainties of the average parameters given in Table 2 the total upstream and downstream energy fluxes agree to within 3%. Certainly this level of agreement is fortuitous rather than a testament to the robustness of the accuracy of any parameter value. For example, over the averaging interval used for the Wind solar wind data, the proton density varies from 4.0 to 5.0 particles/cm$^3$. Determining the "best" lag time from Wind to the bow shock depends either on assumptions about convection speeds and orientation of structures or cross-correlating some feature in, say, the magnetic field direction with in our case the MMS spacecraft upstream of the bow shock. Here, we chose to rely instead on mass conservation calculated form the downstream mass flux and solar wind velocity. This calculation agrees with the density deduced directly from the plasma upper hybrid line at Wind, which was 5.3 particles/cm$^3$. This spread in density estimates of 20% or more reflects the expected uncertainty in the primary ram energy. We also used MMS2, the most

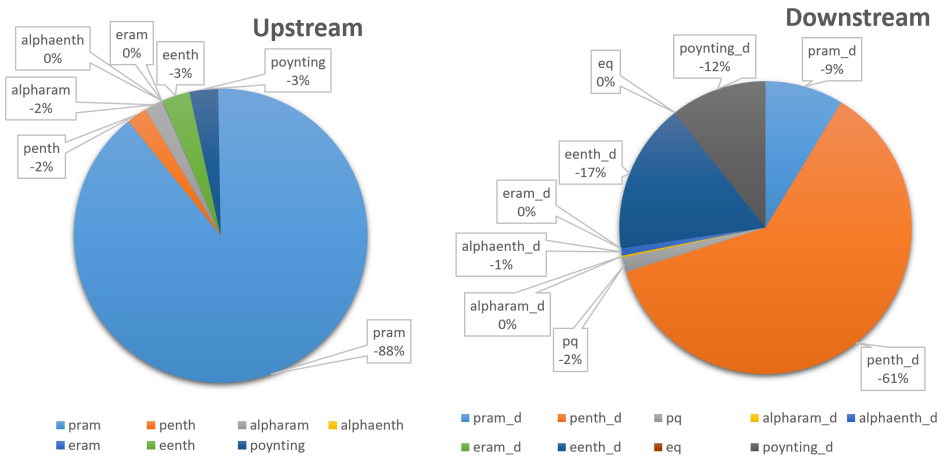


**Figure 1.** Partition of energy fluxes upstream (left) and downstream (right) of the shock crossing on 2019-03-05 derived using the parameter values in Table 2. The total observed energy flux is -193 $\mu W/m^2$ upstream and -199 $\mu W/m^2$ downstream.

upstream spacecraft, to measure the upstream magnetic field as the field direction varies considerably over the distance from Wind at L1 to the bow shock.

Not surprisingly, the upstream energy flux is dominated by the proton ram energy, especially in this case of relatively low $\alpha$ particle density $n_\alpha \sim 0.5\% n_p$. For $\alpha$ particle densities of a few % their ram energy might contribute 10% of the total energy flux. That proton ram energy is converted primarily into the proton enthaply flux observed downstream. Apart from the remnant proton ram energy, the remainder of the energy budget is consumed by the electron energy and a significant DC Poynting flux. Recall that these average values use $\mathbf{E} = -\langle \mathbf{u}'_p \rangle \times \langle \mathbf{B} \rangle$ and thus do not include wave or turbulent fluctuations.

### 4.2 Instantaneous energy fluxes

In addition to evaluating (13) using basic upstream and downstream average parameter values, we also explore the instantaneous energy fluxes making use of the MMS instrument suite. We have not attempted to force the MMS data to match the parameters given in Table 2 which relied on other spacecraft, mass conservation, and other considerations. By following different energy fluxes through the shock, the time series approach provides insight to the processes responsible for the energy (re)partition.

An overview of this shock and the basic energy fluxes is given in Figure 2. As expected, the proton ram energy dominates the upstream (latter half). In the downstream, the proton enthalpy flux is the largest single contribution to the total energy flux, while the electron enthalpy and Poynting fluxes contribute the rest in roughly equal measure. The upstream oscillations are largely the consequence of the solar wind beam moving across pixels in the FPI instrument. Downstream fluctuations may be real but may also be limited by instrumental characteristics. The Poynting flux reaches large values with significant positive and negative excursions within the shock overshoot region just after 19:39.

The dashed horizontal line in Figure 2e shows the energy flux based on the average parameters in Table 2 against the instantaneous total (cyan) that is derived without further correction or assumption from the MMS data. The two approaches appear to agree although the data is subject to large fluctuations. Some of these fluctuations, such as the large variability in upstream ion density, are the result of the instrumental inability to resolve the cold solar wind beam. As we shall see below, some may also be the result of counting statistics of the suprathermal particles. Some of the fluctuations are undoubtedly real and show the influence of turbulence and nonstationarity.

The time series reveal several interesting features. The proton enthalpy flux (red in panel (e)) rises in the shock foot region upstream of the shock ramp. This is due to the presence of reflected protons that effectively broaden the proton distribution there. The rise in proton enthalpy is balanced to some extent by the oppositely-signed proton heat flux (dark green panels (e) and (f)) that is linked to the counter-streaming reflected protons. Within the shock overshoot region there is a systematic decrease in the proton enthalpy flux (panel (e); see also panel (h)) that is compensated by a rise in proton heat flux (panels (e) and (f). At the kinetic level, the tight mutual gyration of transmitted and returning reflected protons results in a proton distribution that is complex and fragmented, resulting in significant anisotropies (discussed below) and distortions. If we treat all the protons as a single species, a significant fraction of the proton energy flux is carried as heat flux. It is possible to regard the protons as having multi-components (Goldman et al., 2020) which would redistribute part of the heat flux to ram or enthaply fluxes of those components. Such a representation does not, of course, change the overall energy flux but it does serve to reveal the physical mechanisms at work that are masked by the moments from the full, single proton population.

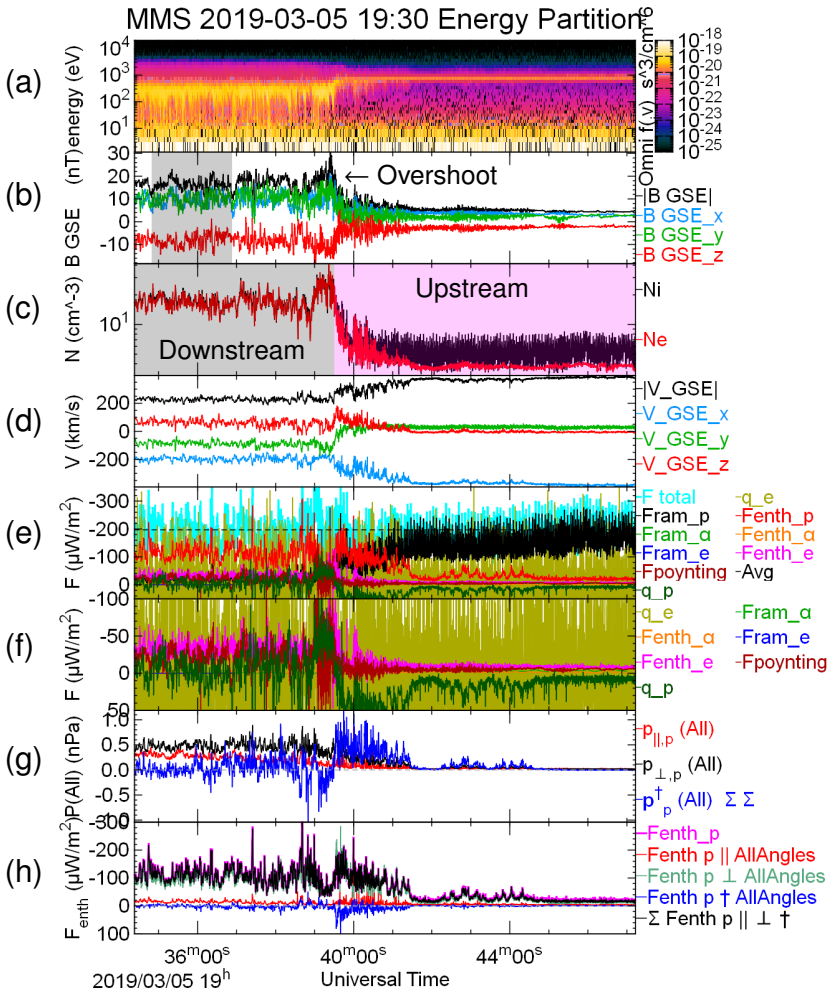


**Figure 2.** Overview of the quasi-perpendicular shock crossing on 2019/03/05 as observed by MMS 1. From top to bottom: (a) ion omnidirectional phase space density (b) magnetic field. The shaded region denotes the interval used to determine downstream average parameters (c) electron and ion (assumed proton) density. The shaded intervals divide the crossing into upstream and regions to which we have applied separate ion "core" and suprathermal masks in later more detailed analysis. (d) ion velocity (e) normal component of the ram and enthalpy fluxes of the protons, alpha particles, and electrons together with the proton and electron heat fluxes and the Poynting flux. The dashed black line corresponds to the average up and downstream total energy flux derived from the parameters in Table 2 while the cyan curve shows the sum of the individual MMS 1 contributions to the instantaneous energy flux. (f) Detail of the fluxes in (e) but omitting the dominant proton ram and enthalpy energy fluxes. (g) decomposition of the proton pressure tensor as computed by us over "All" angles into parallel ($p_{\parallel}$), perpendicular ($p_{\perp}$) and remainder ($\underline{\underline{p}}^{\dagger}$, summed over all elements). (h) Contributions of the decomposed pressure tensor to the proton enthalpy flux as prescribed by (10)-(12) together with their sum and the undecomposed total (magenta) based on L2 data files shown in (e).

Figure 2f confirms the relative importance of the electron enthalpy and Poynting fluxes in the downstream region. Note here that the time series Poynting flux uses instantaneous direct measurements of the DC electric field transformed to the NIF frame and magnetic field, and thus captures all the contributions up to the sampling frequency of the DC magnetometer, namely 128 Hz. The electron heat flux (olive green in panels (e) and (f)) is highly variable. This is probably the result of low count rates in the wings of the electron distribution which dominate the third moment of the electron distribution. It is worth recalling that the solar wind flow is sub-thermal for the electrons, so their distribution is quite broad with only marginal shift due to the bulk motion. Thus, although the electron ram energy is small, the electron enthaply flux plays a significant role downstream.

### 4.3 Anisotropies

Under quasi-perpendicular geometry the primary energy conversion process at supercritical shocks involves a sub-population of incident protons. This subpopulation is near-specularly reflected at the shock ramp and gyrates upstream before crossing into the downstream region where it forms partial ring features in velocity space (Woods, 1969; Paschmann et al., 1982). This spread in velocities is thus primarily perpendicular to the magnetic field. As Figure 2g shows, the perpendicular pressure dominates the downstream region while in the immediate vicinity of the shock ramp the reflected ions are highly agyrotropic; their influence is seen in the large $\underline{\underline{\mathbf{p}}}^{\dagger}$ deviations from the simple $p_{\parallel}$, $p_{\perp}$ parts of the pressure tensor in (7).

There is a very systematic increase in $p_{\parallel}$ from the shock ramp into the downstream region seen in the red trace of Figure 2g. This increase in $p_{\parallel}$ suggests that the protons relax toward isotropy. However, the parallel contribution to the proton enthalpy flux in Figure 2h remains small throughout, as anticipated in the discussion of (10)–(12) above.

### 4.4 Sub-population analysis

The influence of agyrotropy and suprathermal reflected ions suggest that deeper analysis of the ion velocity space distributions and isolation of sub-populations may shed further light on the partition problem. Figure 3 illustrates several analysis strands. Panels (B)–(D) show reduced velocity-time spectrograms after transforming to the NIF frame

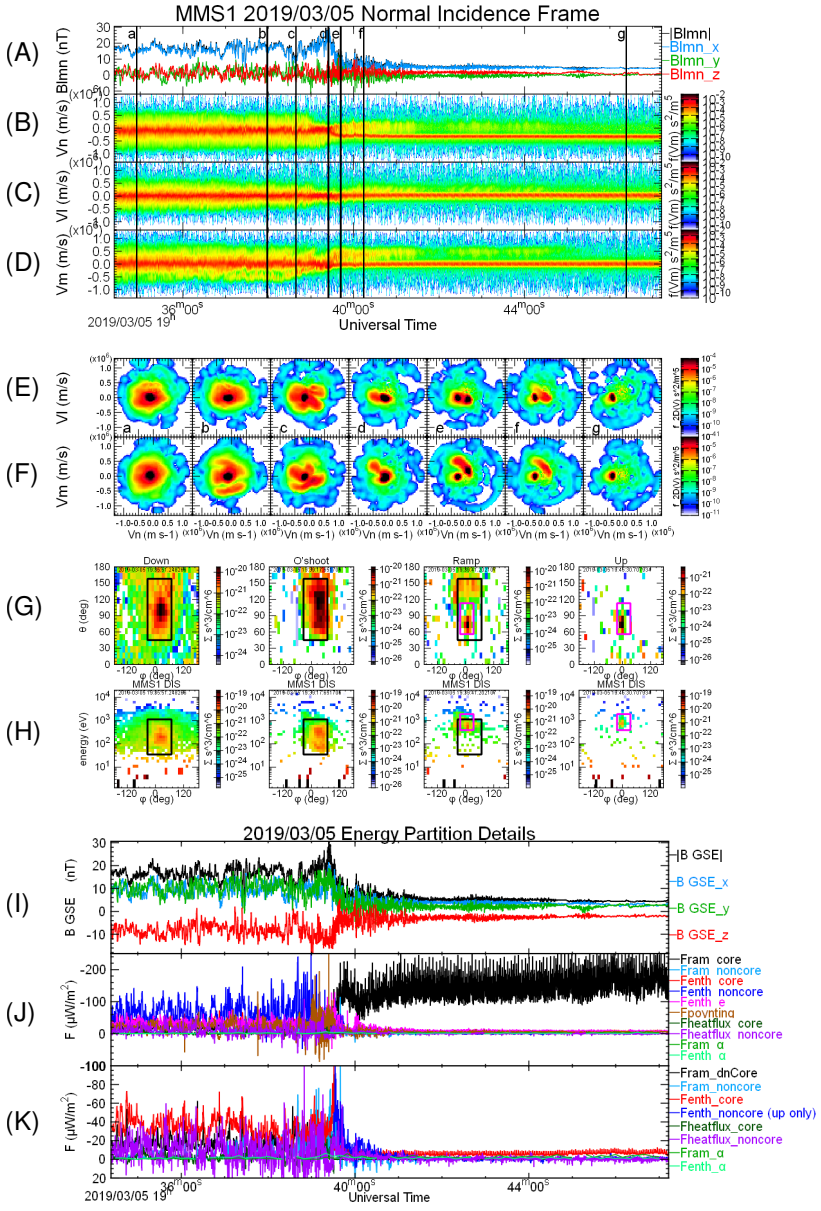


**Figure 3.** Details of the ion distributions and their contributions to the energy fluxes. (A) magnetic field in shock *lmn* coordinates. (B)-(D) ion distributions transformed to the shock normal coordinates and reduced to 1D distributions along the $n$, $m$, and $l$ directions respectively. (E),(F) 1s averaged 2D cuts of ion distributions summed onto the $nl$, $nm$ planes at the times indicated by the vertical lines in (A)-(D). (G) angle-angle and (H) energy-angle reductions of ion distributions downstream, within the overshoot and ramp, and upstream. The black (magenta) boxes isolate the core sub-region in phase space to separate that core from the suprathermals in the downstream (upstream) regions as shaded in Figure 2c. Both sets are shown in Ramp plot to emphasize their relative positions. (I) DC magnetic field (J) energy fluxes along the shock normal for the separate core and non-core ions together with the Poynting flux and (negligibly small) $\alpha$ particle energy fluxes. (K) detail of (J) omitting the upstream ram and downstream noncore enthalpy fluxes.

and rotating into shock normal coordinates. Here $n$ is the upstream-directed normal component, the upstream magnetic field lies in the $nl$ plane with $B_l > 0$ and $m$ completes the right-handed system. In addition to the incident solar wind beam at $V_n < 0$ seen continuously after ∼19:40, the reflected ions ($V_n > 0$) are visible upstream of the shock ramp in panel B, and also in the $V_m$ spectrograms (panel D) both upstream and downstream.

The reflected ions are seen in the snapshots of the 2D reduced distributions in (E), (F). In (F)f, for example, they appear as the extended arc above and right of the small intense solar wind beam. These reflected ions remain distinct even downstream of the shock and evolve from the simple velocity space portraits in, e.g., (E)f, (F)f. As noted previously, the ion distributions within the overshoot region, marked (d) in (A)–(F) are noticeably less dispersed in velocity space with a depletion at suprathermal velocities relative to the distributions further downstream. We note here that while the spatial size of a gyro-orbit will decrease in a strong $|\mathbf{B}|$ region, its velocity should not. The overshoot region is unusual in that no one or two energy fluxes dominate here. This region also appears to be a barrier to the downstream suprathermal protons.

To explore the relative energy flux contributions of the core protons and reflected or suprathermal protons we have isolated the core population in velocity space by the central delineated region Figure 3G,H. This core embodies the primary thermal protons. The "noncore" population of suprathermal or otherwise nonthermal protons occupy the remainder of velocity space outside the central core region. We employ simple instrumental masks for this purpose, using different masks downstream (black) and upstream (magenta) corresponding to the regions shown in Figure 2c. We then treat these as two sub-populations and calculate their moments and resulting contributions to the terms in (13) which are shown in panels J and K.

In the downstream region, and in the shock foot, the proton enthalpy flux is carried primarily by the noncore protons (blue trace). Downstream the noncore protons are ∼18% of the total population and carry 60% of the proton enthalpy flux, or 40% of the total energy flux. Panel K omits non-core flux downstream to uncover the core proton enthalpy flux (red) which is roughly half as large. The residual intrinsic heat flux of the noncore component (purple) is highly variable but on average is ∼75% of the downstream

core ram energy flux (black), indicating that the noncore protons contribute this additional energy flux to the downstream energy budget.

## 5 Example 2: 2019-02-15 at 10:22

We have similarly analyzed another example drawn from the season in which the MMS spacecraft were strung out in a colinear configuration with total separation ∼700 km. In this case, the shock motion was less steady but moving sunward at a speed of ∼54 km/s based on the average of speeds deduced from the successive ramp crossings by the 4 spacecraft. The upstream plasma $\beta$'s were $\beta_{i,e} = 0.55, 0.77$, only slightly higher than the first example. The Alfvén and fast Mach numbers were also slightly higher at 8.9 and 6.1 respectively. The shock was very nearly perpendicular ($\theta_{Bn} = 93°$). One significant difference is that the solar wind $\alpha$-particle density at 1.7% that of the protons was closer to average solar wind values.

An overview of this shock, and the resulting energy fluxes, is shown in Figure 4 in the same format as Figure 2. Panels (i) and (j) show the energy partition at this shock deduced from average values upstream and downstream as shaded in (b) and supplemented by more accurate solar wind parameters from Wind and tweaked to ensure mass conservation. In this case, similar assumptions to those footnoted in Table 2 yield an average total energy flux of 309 $\mu$W/m$^2$ which agree to within 3% from upstream to downstream. The energy flux is 50% larger in this case, due to a combination of the faster and outward shock speed, a higher solar wind velocity (460 km/s), larger plasma $\beta$ and higher $\alpha$-particle density. Here the $\alpha$ ram energy contributes 6% of the total upstream energy flux.

This example also shows the role played by proton agyrotropies and anisotropies within the overshoot and downstream. The distorted proton distributions in the shock ramp and overshoot manifest themselves in significant contributions from the proton heat flux and $\underline{\underline{\mathbf{p}}}^{\dagger}$. Downstream the perpendicular enthalpy flux dominates despite the similar parallel and perpendicular pressures. With higher energy fluxes and plasma $\beta$, it becomes harder to separate systematically core vs. non-core proton distributions downstream of the shock.

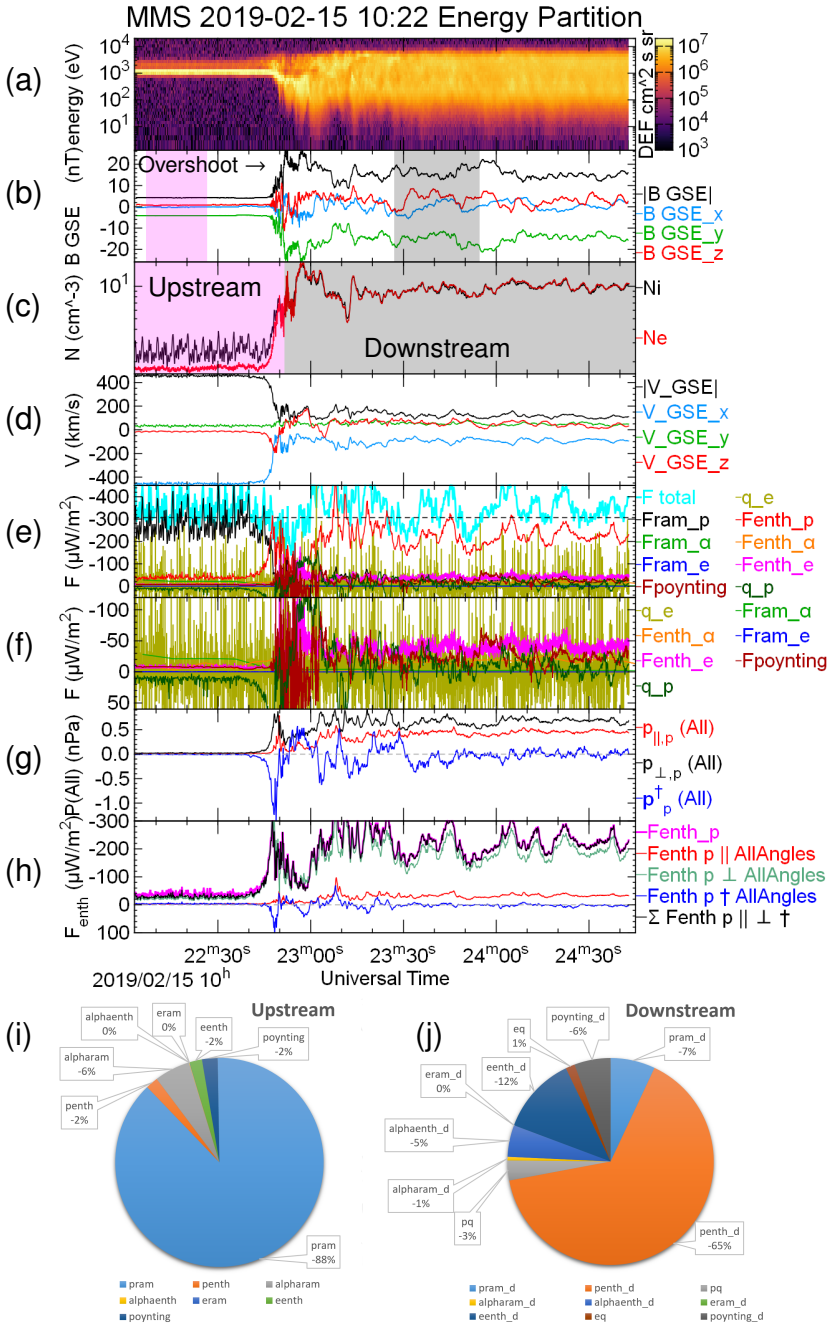


**Figure 4.** (a)-(h)As in Figure 2 but for the nearly perpendicular shock crossing at 10:22 on 2019-02-15 except (a) plots differential energy flux. Shaded regions in (b) were used to compute some average upstream and downstream parameters (i)-(j) Energy partition pie charts.

## 6 Instrumental considerations

The analysis presented here makes strong demands on the resolution of the instrumentation. We have already mentioned the MMS FPI design constraints which prevent it from fully resolving the cold solar wind ions (see also Cara et al., 2017; De Keyser et al., 2018; De Marco et al., 2016). This constraint is illustrated by the small number of pixels within the core mask shown in the rightmost plots of Figure 3G,H. Virtually all the nonzero pixels outside that mask in the far upstream region correspond to a single count. Note that these occur over all energies due to a combination of low phase space density and background sources. The omni-directional phase space distribution in Figure 2 illustrates the problem at low energies where in the upstream region the phase space density should be very low. The noise floor also impinges at high energies, well-above the solar wind beam.

Although uncertainties due to counting statistics are quantified (Gershman et al., 2015), they lead to low signal-to-noise ratio in the data. For our own moment calculations we remove bins below 25 eV in the spacecraft frame to minimize the impact on the energy fluxes. The same issues are also probably responsible for the broad low-level background seen in the reduced ion distributions (e.g., Figure 3E,F) for which we did not attempt to remove low signal-to-noise bins.

FPI electron measurements can become starved for counts at the lowest energies, where careful removal of photo- and secondary electrons is required along with adjustment for the spacecraft potential. Errors and uncertainties in these pre-processing procedures propagate in particular to the low order electron moments, i.e., the density and velocity. At high energies where phase space densities are low, electron count rates are also be small. Since high energies contribute disproportionately to higher particle moments, errors and noise here impact directly the determination of the electron energy fluxes. For example, in our case studies, the electron intrinsic heat fluxes are highly variable. Improving the signal-to-noise at high energies, for both electrons and ions, within a single detector would involve increasing the dynamic ragne to cope with the disparate characteristics of the solar wind and magnetosheath plasmas.

In addition to these counting and background matters, the FPI instrument employs a deflector system to enable a full $2\pi$ range of azimuthal directions to be sampled within the instrument's 150 ms ion sample period. The sequence of deflector sweeps competes

with the spacecraft spin to generate instrumental periocities of $\sim 0.5-2.5\,\mathrm{s}$ (Barrie et al., 2021). Combined with the coarse sampling grid, the energy-angle sampling pattern catches a varying part of the solar wind peak resulting in the large fluctuations seen in the density there. Additionally, some of the variability of the downstream energy fluxes calculated here may contain remnants of this instrumental characteristic particularly when looking at details of sub-populations or anisotropies.

We have utilized $\alpha$-particle measurements from MMC HPCA. This instrument also has difficulty resolving the cold solar wind beam upstream of the shock, compounded by low count rates there. The $\alpha$'s carry a substantial energy flux in the solar wind. Through the shock layer where fields are tuned to process the primary influx of protons, they behave differently due to their higher mass to charge ratio (Burgess, 1989; Fuselier et al., 1988; Trattner & Scholer, 1993; Gedalin, 2017; Madanian, Schwartz, et al., 2021). Analyzing the evolution of anisotropies and sub-populations through the shock ramp will require next generation composition instrumentation capable of coming closer to the cadence of proton measurements.

## 7 Conclusions

The physics of collisionless shocks results in a partition of the incident energy that has not been systematically assessed to date. It has implications not only for determining the primary heating of, e.g., protons and electrons, but also for generating turbulence, accelerating sub-populations of particles, and influencing the minor species. Here we have laid out systematically the formalism to undertake this task. We began here with the simplest examples, namely reasonably steady moderate Mach number terrestrial bow shocks observed with the comprehensive state-of-the-art instrumentation onboard the MMS spacecraft. We also selected two quasi-perpendicular or perpendicular shocks. These are the most familiar, the most studied and simulated and also, thanks to the order imposed by the dominant magnetic field component tangential to the shock surface, the cleanest examples of collisionless shocks.

The application of the formalism is not without its difficulties. Most of these, in the present examples, can be traced to limitations in instrument suites not designed to simultaneously resolve the cold super-thermal solar wind proton beam and the hot shocked magnetosheath ions. Both ion and electron measurements can be compromised by low

densities and contamination. Low count rates at low energies, due to the standard energy-dependent response, and at high energies, due to low phase space densities, require care to recover accurately the full set of plasma moments up to and including particle heat fluxes. Lower cadence and signal-to-noise for the composition instrumentation adds uncertainty in quantifying the input and response of minor species, of which the solar wind $\alpha$-particles represent significant energy carriers.

The Poynting flux is an important energy carrier. While we have not highlighted its measurement, calibrating magnetic and especially 3D electric field instruments from DC to kinetic frequencies requires the level of care and sophistication adopted by the MMS FIELDS team. Here the unequal length of spin-plane and axial electric antennae pose one of several obstacles to be overcome.

We have focused on expanding the particle energy flux into component ram, enthalpy, and intrinsic heat flux contributions. Those can be cast in different ways, including sub-dividing the particle populations into core and non-core elements, and decomposing the full pressure tensor into components parallel and perpendicular to the local magnetic field, together with a remnant tensor that holds information on shears, agyrotropies and other aspects that cannot be captured in the simple parallel-perpendicular paradigm.

We have performed two complementary analyses. To characterize the top-level energy partition, we have identified parameter values representative of the undisturbed region ahead of the shock and the downstream shocked plasma, on the assumption that both the shock and the solar wind conditions remain steady throughout. We exploited an MMS campaign in which the 4 spacecraft were stretched along a line, and hence roughly along the shock normal given the MMS high apogee elliptical orbit, to aid in selecting such cases. We filled in gaps or uncertainties in MMS data by comparing it to data from the Wind spacecraft far upstream. Such comparisons are often made, but not without adding uncertainty both due to the long (40 mins) advection time and to the different instruments operated by the two missions. In some cases we substituted average values for inaccessible parameters, assumed mass conservation across the shock to estimate the poorly-determined solar wind density, and other educated-guess determinations as described in the extensive footnotes to Table 2.

As an alternative, and to probe the microphysics responsible for the energy partition, we calculated instantaneous values of all the contributing energy fluxes from upstream through the shock transition to downstream. For this purpose, we drew uniquely from the level 2 science quality data available in the public MMS archives. Surprisingly, the total energy flux deduced this way agrees to that in the top-level average approach to within 3%. We regard this agreement as fortuitous rather than definitive. This time series analysis reveals large fluctuations in most, if not all, parameters and fluxes. While some of these fluctuations are real, some can certainly be traced to the instrument limitations discussed above.

Although we have concentrated on illustrating the concepts via two relatively simple examples, we can already draw some conclusions about the energy partition at quasi-perpendicular shocks. Some of these were previously known or suspected but others less so. These include:

1. The perpendicular proton pressure dominates the proton enthalpy flux even if the parallel pressure is nearly the same.
2. In the shock foot, ramp and overshoot regions the proton energy flux includes contributions from non-gyrotropic elements of the pressure tensor ($\underline{\underline{\mathbf{p}}}^{\dagger}$ in our terminology) and from the intrinsic proton heat flux. These contributions are traced to the multiple proton sub-populations of transmitted and reflected ions.
3. In the downstream region, the main core protons comprise over 80% of the population but carry only 40% of the proton enthalpy flux. The noncore, i.e. suprathermal, protons are responsible for over 40% of the total energy flux even farther downstream.
4. The total downstream proton enthalpy flux carries over 60% of the downstream energy flux, followed by the electron enthalpy flux at 12–17% depending on the presence of a significant $\alpha$-particle population.
5. In our example with significant $\alpha$'s (1.7%) by number, their ram energy flux is 6% of the total upstream energy budget while their downstream enthalpy flux is 5% of the total. The $\alpha$'s are the second highest element of the incident energy in this case. Their contribution would scale linearly under more extreme $\alpha$-rich conditions.

6. The downstream region exhibits large quasi-periodic fluctuations in total energy flux even under these relatively stable conditions.

The same framework is useful for studying the energy partition at quasi-parallel shocks. Such shocks present at least two new aspects. Firstly, they are known to be inherently time-dependent, with large amplitude fluctuations in both fields and particle quantities extending from the foreshock region well into the downstream. It is possible, of course, to apply the same full time series analysis we performed in the present work to quasi-parallel shocks, but attempting to separate the contributions of fluctuations vs. quasi-steady parameters will require some care. Additionally, and importantly, quasi-parallel shocks are known particle accelerators. The energy carried away by energetic particles and its dependence on shock parameters is an important aspect of collisionless shock physics (David et al., 2022). Thus while in the present study we have neglected energetic particles, they could and will need to be included within the same framework.

While progress can be made with data from existing space assets, this work has also highlighted current limitations. Foremost amongst these is the need to fully resolve the incident cold solar wind proton beam, and to be able to similarly measure the most important minor ions, especially the $\alpha$-particles. Such measurements will need to be well-matched to full $4\pi$ coverage of the heated downstream populations. The ion distributions at and downstream of the shock are highly fragmented which places demands on both the temporal and angular/energy resolution required to capture the underlying physics correctly. We have also seen here the importance of suprathermal wings of both ion and electron distributions, with corresponding requirements to improve count rates in those regions of phase space. Finally, simultaneous measurements upstream and downstream would facilitate shock studies under more variable interplanetary conditions. Some studies may be made possible by larger separations of the MMS spacecraft. We look forward to the eventual selection of a mission such as MAKOS (Multi-point Assessment of the Kinematics of Shocks) that can overcome present limitations.

**Acknowledgments**

Wind data were drawn from the SPDF/CDAWEB repository (`https://cdaweb.gsfc.nasa.gov/index.html/`). We gratefully acknowledge the respective instrument teams and archive curators. MMS data can be found at the MMS public Science Data Cen-

ter (`https://lasp.colorado.edu/mms/sdc/public/`). Data analysis and graphics were performed using the opensource QSAS Science Analysis System (`https://sourceforge.net/projects/qsas/`). Some of the work was supported by the International Space Science Institute's (ISSI) International Teams programme ("Resolving the Microphysics of Collisionless Shock Waves" led by L.B. Wilson III) and the Geospace Environment Modeling (GEM) Focus Group "Particle Heating and Thermalization in Collisionless Shocks in the MMS Era" led by L.B. Wilson III. This work was supported by NASA Awards 80NSSC19K0849 and 80NSSC20K0688 together with NASA MMS contracts to the instrument teams.

## References

Amano, T., Katou, T., Kitamura, N., Oka, M., Matsumoto, Y., Hoshino, M., ... Blake, J. B. (2020, February). Observational Evidence for Stochastic Shock Drift Acceleration of Electrons at the Earth's Bow Shock. *Phys. Rev. Lett.*, *124*(6), 065101. doi: 10.1103/PhysRevLett.124.065101

Barrie, A. C., Schiff, C., Gershman, D. J., Giles, B. L., & Rand, D. (2021, July). Calibrating Electrostatic Deflection of Charged Particle Sensors Using Ambient Plasma Measurements. *J. Geophys. Res.*, *126*(7), e29149. doi: 10.1029/2021JA029149

Boyd, T. J. M., & Sanderson, J. J. (2003). *The physics of plasmas.* doi: 10.1017/cbo9780511755750

Burch, J. L., Moore, T. E., Torbert, R. B., & Giles, B. L. (2016, March). Magnetospheric Multiscale Overview and Science Objectives. *Space Sci. Rev.*, *199*, 5-21. doi: 10.1007/s11214-015-0164-9

Burgess, D. (1989, February). Alpha particles in field-aligned beams upstream of the bow shock: Simulations. *Geophys. Res. Lett.*, *16*(2), 163-166. doi: 10.1029/GL016i002p00163

Burgess, D., & Scholer, M. (2015). *Collisionless Shocks in Space Plasmas.* Cambridge University Press.

Cara, A., Lavraud, B., Fedorov, A., De Keyser, J., DeMarco, R., Marcucci, M. F., ... Bruno, R. (2017, February). Electrostatic analyzer design for solar wind proton measurements with high temporal, energy, and angular resolutions. *Journal of Geophysical Research (Space Physics)*, *122*(2), 1439-1450. doi:

10.1002/2016JA023269

David, L., Fraschetti, F., Giacalone, J., Wimmer-Schweingruber, R. F., Berger, L., & Lario, D. (2022, February). In-situ Measurement of the Energy Fraction in Supra-thermal and Energetic Particles at ACE, Wind, and PSP Interplanetary Shocks. *arXiv e-prints*, arXiv:2202.11029.

De Keyser, J., Lavraud, B., Přech, L., Neefs, E., Berkenbosch, S., Beeckman, B., ... Brienza, D. (2018, October). Beam tracking strategies for fast acquisition of solar wind velocity distribution functions with high energy and angular resolutions. *Ann Geophys*, *36*(5), 1285-1302. doi: 10.5194/angeo-36-1285-2018

De Marco, R., Marcucci, M. F., Bruno, R., D'Amicis, R., Servidio, S., Valentini, F., ... Salatti, M. (2016, August). Importance of energy and angular resolutions in top-hat electrostatic analysers for solar wind proton measurements. *Journal of Instrumentation*, *11*(8), C08010. doi: 10.1088/1748-0221/11/08/C08010

Ergun, R. E., Tucker, S., Westfall, J., Goodrich, K. A., Malaspina, D. M., Summers, D., ... Cully, C. M. (2016, March). The Axial Double Probe and Fields Signal Processing for the MMS Mission. *Space Sci. Rev.*, *199*, 167-188. doi: 10.1007/s11214-014-0115-x

Fuselier, S. A., Shelley, E. G., Balsiger, H., Geiss, J., Goldstein, B. E., Goldstein, R., & Ip, W. H. (1988, June). Cometary $H_2^+$ and solar wind $He^{2+}$ dynamics across the Halley cometopause. *Geophys. Res. Lett.*, *15*(6), 549-552. doi: 10.1029/GL015i006p00549

Gedalin, M. (2017, January). Effect of alpha particles on the shock structure. *J. Geophys. Res.*, *122*(1), 71-76. doi: 10.1002/2016JA023460

Gedalin, M. (2020, May). Large-scale versus Small-scale Fields in the Shock Front: Effect on the Particle Motion. *Astrophys. J.*, *895*(1), 59. doi: 10.3847/1538-4357/ab8af0

Gershman, D. J., Dorelli, J. C., F. -Viñas, A., & Pollock, C. J. (2015, August). The calculation of moment uncertainties from velocity distribution functions with random errors. *J. Geophys. Res.*, *120*(8), 6633-6645. doi: 10.1002/2014JA020775

Gingell, I., Schwartz, S. J., Eastwood, J. P., Burch, J. L., Ergun, R. E., Fuselier, S., ... Wilder, F. (2019, February). Observations of Magnetic Reconnection in the Transition Region of Quasi-Parallel Shocks. *Geophys. Res. Lett.*, *46*(3),

1177-1184. doi: 10.1029/2018GL081804

Gingell, I., Schwartz, S. J., Eastwood, J. P., Stawarz, J. E., Burch, J. L., Ergun, R. E., ... Wilder, F. (2020, January). Statistics of Reconnecting Current Sheets in the Transition Region of Earth's Bow Shock. *J. Geophys. Res.*, *125*(1), e27119. doi: 10.1029/2019JA027119

Goldman, M. V., Newman, D. L., Eastwood, J. P., & Lapenta, G. (2020, December). Multibeam Energy Moments of Multibeam Particle Velocity Distributions. *J. Geophys. Res.*, *125*(12), e28340. doi: 10.1029/2020JA028340

Goldman, M. V., Newman, D. L., Eastwood, J. P., Lapenta, G., Burch, J. L., & Giles, B. (2021, October). Multi-beam energy moments of measured compound ion velocity distributions. *Phys Plasmas*, *28*(10), 102305. doi: 10.1063/5.0063431

Goodrich, K. A., Ergun, R., Schwartz, S. J., Wilson, L. B., Newman, D., Wilder, F. D., ... Andersson, L. (2018, November). MMS Observations of Electrostatic Waves in an Oblique Shock Crossing. *J. Geophys. Res.*, *123*(11), 9430-9442. doi: 10.1029/2018JA025830

Harten, R., & Clark, K. (1995, February). The Design Features of the GGS Wind and Polar Spacecraft. *Sp. Sci. Rev.*, *71*(1-4), 23-40. doi: 10.1007/BF00751324

Johlander, A., Vaivads, A., Khotyaintsev, Y. V., Gingell, I., Schwartz, S. J., Giles, B. L., ... Russell, C. T. (2018). Shock ripples observed by the MMS spacecraft: ion reflection and dispersive properties. *Plasma Phys. Control. Fusion*, *60*, 125006. doi: 10.1088/1361-6587/aae920

Kis, A., Scholer, M., Klecker, B., Möbius, E., Lucek, E. A., Rème, H., ... Kucharek, H. (2004, October). Multi-spacecraft observations of diffuse ions upstream of Earth's bow shock. *Geophys. Res. Lett.*, *31*(20), L20801. doi: 10.1029/2004GL020759

Krasnoselskikh, V., Balikhin, M., Walker, S. N., Schwartz, S. J., Sundkvist, D., Lobzin, V., ... Comisel, H. (2013, October). The Dynamic Quasiperpendicular Shock: Cluster Discoveries. *Sp. Sci. Rev.*, *178*(2-4), 535-598. doi: 10.1007/s11214-013-9972-y

Kucharek, H., Möbius, E., Li, W., Farrugia, C. J., Popecki, M. A., Galvin, A. B., ... Bochsler, P. A. (2003, October). On the source and acceleration of energetic $He^+$: A long-term observation with ACE/SEPICA. *J. Geophys. Res.*,

*108*(A10), 8040. doi: 10.1029/2003JA009938

Kucharek, H., Möbius, E., Scholer, M., Mouikis, C., Kistler, L., Horbury, T., ... Bosqued, J. (2004, July). On the origin of field-aligned beams at the quasi-perpendicular bow shock: multi-spacecraft observations by Cluster. *Ann Geophys*, *22*(7), 2301-2308. doi: 10.5194/angeo-22-2301-2004

Leroy, M. M., Winske, D., Goodrich, C. C., Wu, C. S., & Papadopoulos, K. (1982, July). The structure of perpendicular bow shocks. *J. Geophys. Res.*, *87*(A7), 5081-5094. doi: 10.1029/JA087iA07p05081

Lindqvist, P.-A., Olsson, G., Torbert, R. B., King, B., Granoff, M., Rau, D., ... Tucker, S. (2016, March). The Spin-Plane Double Probe Electric Field Instrument for MMS. *Space Sci. Rev.*, *199*, 137-165. doi: 10.1007/s11214-014-0116-9

Lowe, R. E., & Burgess, D. (2003, March). The properties and causes of rippling in quasi-perpendicular collisionless shock fronts. *Annales Geophysicae*, *21*(3), 671-679. doi: 10.5194/angeo-21-671-2003

Madanian, H., Desai, M. I., Schwartz, S. J., Wilson, I., L. B., Fuselier, S. A., Burch, J. L., ... Lindqvist, P. A. (2021, February). The Dynamics of a High Mach Number Quasi-perpendicular Shock: MMS Observations. *Astrophys. J.*, *908*(1), 40. doi: 10.3847/1538-4357/abcb88

Madanian, H., Schwartz, S. J., Fuselier, S. A., Burgess, D., Turner, D. L., Chen, L.-J., ... Starkey, M. J. (2021, July). Direct Evidence for Magnetic Reflection of Heavy Ions from High Mach Number Collisionless Shocks. *Astrophys. J. Lett.*, *915*(1), L19. doi: 10.3847/2041-8213/ac0aee

Paschmann, G., & Daly, P. W. (2008). Notes on "ISSI SR-001". In *Multi-Spacecraft Analysis Methods Revisited* (p. xi). ESA Communications for The International Space Science Institute.

Paschmann, G., Sckopke, N., Bame, S. J., & Gosling, J. T. (1982, August). Observations of gyrating ions in the foot of the nearly perpendicular bow shock. *Geophys. Res. Lett.*, *9*(8), 881-884. doi: 10.1029/GL009i008p00881

Pollock, C., Moore, T., Jacques, A., Burch, J., Gliese, U., Saito, Y., ... others (2016, March). Fast Plasma Investigation for Magnetospheric Multiscale. *Space Sci. Rev.*, *199*, 331-406. doi: 10.1007/s11214-016-0245-4

Russell, C. T., Anderson, B. J., Baumjohann, W., Bromund, K. R., Dearborn,

D., Fischer, D., ... Richter, I. (2016, March). The Magnetospheric Multiscale Magnetometers. *Space Sci. Rev.*, *199*, 189-256. doi: 10.1007/s11214-014-0057-3

Schwartz, S. J. (1998, January). Shock and Discontinuity Normals, Mach Numbers, and Related Parameters. *ISSI Scientific Reports Series*, *1*, 249-270.

Schwartz, S. J. (2006, June). Shocks: Commonalities in Solar-Terrestrial Chains. *Sp. Sci. Rev.*, *124*(1-4), 333-344. doi: 10.1007/s11214-006-9093-y

Schwartz, S. J., Ergun, R., Kucharek, H., Wilson, L., Chen, L.-J., Goodrich, K., ... Strangeway, R. (2021, August). Evaluating the deHoffmann-Teller Cross-Shock Potential at Real Collisionless Shocks. *J. Geophys. Res.*, *126*(8), e29295. doi: 10.1029/2021JA029295

Schwartz, S. J., & Marsch, E. (1983, December). The radial evolution of a single solar wind plasma parcel. *J. Geophys. Res.*, *88*(A12), 9919-9932. doi: 10.1029/JA088iA12p09919

Schwartz, S. J., Thomsen, M. F., Bame, S. J., & Stansberry, J. (1988, November). Electron heating and the potential jump across fast mode shocks. *J. Geophys. Res.*, *93*, 12923-12931. doi: 10.1029/JA093iA11p12923

Schwartz, S. J., Zweibel, E. G., & Goldman, M. (2013, October). Microphysics in Astrophysical Plasmas. *Sp. Sci. Rev.*, *178*(2-4), 81-99. doi: 10.1007/s11214-013-9975-8

Sckopke, N., Paschmann, G., Bame, S. J., Gosling, J. T., & Russell, C. T. (1983, August). Evolution of ion distributions across the nearly perpendicular bow shock: specularly and non-specularly reflected-gyrating ions. *J. Geophys. Res.*, *88*(A8), 6121-6136. doi: 10.1029/JA088iA08p06121

Scudder, J. D., Mangeney, A., Lacombe, C., Harvey, C. C., & Aggson, T. L. (1986, October). The resolved layer of a collisionless, high $\beta$, supercritical, quasi-perpendicular shock wave. 2. Dissipative fluid electrodynamics. *J. Geophys. Res.*, *91*(A10), 11053-11074. doi: 10.1029/JA091iA10p11053

Scudder, J. D., Mangeney, A., Lacombe, C., Harvey, C. C., Wu, C. S., & Anderson, R. R. (1986, October). The resolved layer of a collisionless, high $\beta$, supercritical, quasi-perpendicular shock wave, 3. Vlasov electrodynamics. *J. Geophys. Res.*, *91*(A10), 11075-11098. doi: 10.1029/JA091iA10p11075

Slavin, J. A., & Holzer, R. E. (1981, December). Solar wind flow about the ter-

restrial planets, 1. Modeling bow shock position and shape. *J. Geophys. Res.*, *86*(A13), 11401-11418. doi: 10.1029/JA086iA13p11401

Stone, R. G., & Tsurutani, B. T. (1985, January). Collisionless shocks in the heliosphere. A tutorial review. *Washington DC American Geophysical Union Geophysical Monograph Series*, *34*. doi: 10.1029/GM034

Torbert, R. B., Russell, C. T., Magnes, W., Ergun, R. E., Lindqvist, P.-A., LeContel, O., ... Lappalainen, K. (2016, March). The FIELDS Instrument Suite on MMS: Scientific Objectives, Measurements, and Data Products. *Space Sci. Rev.*, *199*, 105-135. doi: 10.1007/s11214-014-0109-8

Trattner, K. J., & Scholer, M. (1993, September). Distributions and thermalization of protons and alpha particles at collisionless quasi-parallel shocks. *Ann Geophys*, *11*(9), 774-789.

Tsurutani, B. T., & Stone, R. G. (1985, January). Collisionless shocks in the heliosphere: Reviews of current research. *Washington DC American Geophysical Union Geophysical Monograph Series*, *35*. doi: 10.1029/GM035

Wang, S., Chen, L.-J., Bessho, N., Hesse, M., Wilson, L. B., Giles, B., ... Burch, J. L. (2019, January). Observational Evidence of Magnetic Reconnection in the Terrestrial Bow Shock Transition Region. *Geophys. Res. Lett.*, *46*(2), 562-570. doi: 10.1029/2018GL080944

Wilson, L. B., Brosius, A. L., Gopalswamy, N., Nieves-Chinchilla, T., Szabo, A., Hurley, K., ... TenBarge, J. M. (2021, June). A quarter century of wind spacecraft discoveries. *Rev. Geophys.*, *59*(2), e2020RG000714. doi: 10.1029/2020rg000714

Wilson, L. B., Sibeck, D. G., Breneman, A. W., Le Contel, O., Cully, C., Turner, D. L., ... Malaspina, D. M. (2014, August). Quantified energy dissipation rates in the terrestrial bow shock: 2. Waves and dissipation. *J. Geophys. Res.*, *119*(8), 6475-6495. doi: 10.1002/2014JA019930

Wilson, L. B., III, Chen, L.-J., Wang, S., Schwartz, S. J., Turner, D. L., Stevens, M. L., ... Goodrich, K. A. (2019a, December). Electron Energy Partition across Interplanetary Shocks. II. Statistics. *Astrophys. J. Supp.*, *245*(2), 24. doi: 10.3847/1538-4365/ab5445

Wilson, L. B., III, Chen, L.-J., Wang, S., Schwartz, S. J., Turner, D. L., Stevens, M. L., ... Goodrich, K. A. (2019b, July). Electron Energy Partition across

729 Interplanetary Shocks. I. Methodology and Data Product. *Astrophys. J. Supp.*,
730 *243*(1), 8. doi: 10.3847/1538-4365/ab22bd
731 Wilson, L. B., III, Chen, L.-J., Wang, S., Schwartz, S. J., Turner, D. L., Stevens,
732 M. L., ... Goodrich, K. A. (2020, April). Electron Energy Partition
733 across Interplanetary Shocks. III. Analysis. *Astrophys. J.*, *893*(1), 22. doi:
734 10.3847/1538-4357/ab7d39
735 Wilson, L. B., III, Stevens, M. L., Kasper, J. C., Klein, K. G., Maruca, B. A., Bale,
736 S. D., ... Salem, C. S. (2018, June). The Statistical Properties of Solar Wind
737 Temperature Parameters Near 1 au. *Astrophys. J. Supp.*, *236*(2), 41. doi:
738 10.3847/1538-4365/aab71c
739 Woods, L. C. (1969, September). On the structure of collisionless magneto—plasma
740 shock waves at super—critical Alfvén—Mach numbers. *J. Plasma Phys.*, *3*(3),
741 435-447. doi: 10.1017/S0022377800004517
742 Young, D. T., Burch, J. L., Gomez, R. G., Santos, A. D. L., Miller, G. P., Wilson,
743 P., ... Webster, J. M. (2017). *Hot plasma composition analyzer for the magne-*
744 *tospheric multiscale mission.* doi: 10.1007/978-94-024-0861-4_13
745 Zank, G. P., Nakanotani, M., Zhao, L., Du, S., Adhikari, L., Che, H., & le
746 Roux, J. (2021). Flux ropes, turbulence, and collisionless perpendicu-
747 lar shock waves: High plasma beta case. *Astrophys. J.*, *913*(2), 127. doi:
748 10.3847/1538-4357/abf7c8